3.4 Hardware Design NIRS Module

In this section, the detailed implementation of the system concept's NIRS module elements is described. To do so, the functional units are viewed individually, implemented under consideration of the findings in earlier sections and were built upon another using the results of evaluation and testing of 3 prototype versions. Fig. 3.4 shows two main results of the NIRS module development process.

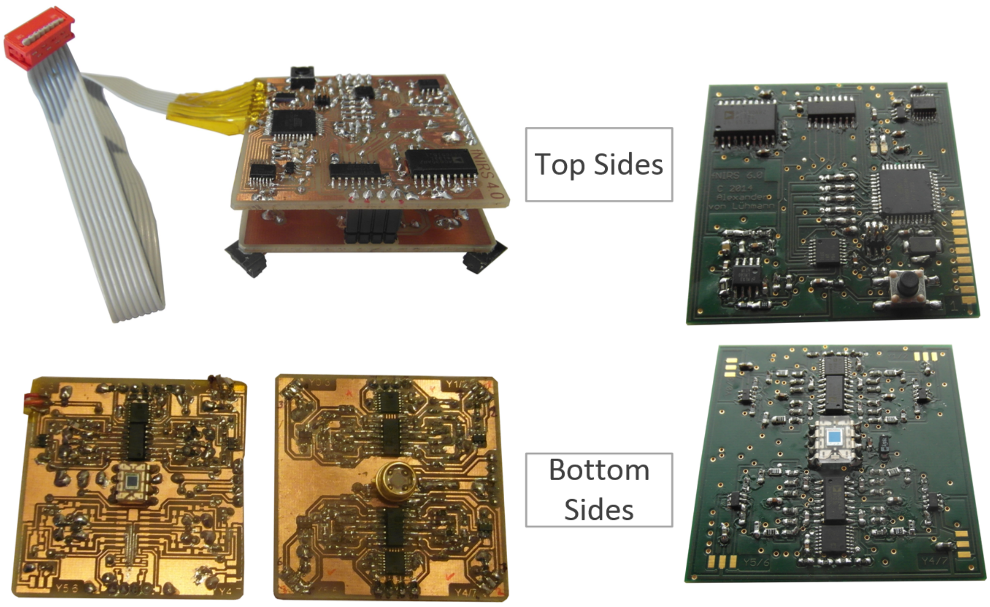

Figure 3.4: NIRS module design steps. Left: prototype with exchangeable sensor PCB, right: final version.

In the prototype version (left), the NIRS module itself is built up from two modules that are plugged onto each other, allowing evaluation of different detector types. On the right, the final 4-layer PCB version of the NIRS module is shown. In the following, the hardware design of this module will be discussed in detail based on excerpts of the final hardware schematics. For the complete schematics, please refer to the appendix figs. A.3 and A.4.

3.4.1 NIR Light Emitter

As described in section 2.5 and contrasted in tab. 2.2, only laser diodes (LD) and light emitting diodes (LEDs) can be used for a mobile and compact instrument.
LDs have the advantages of very sharp radiation peaks and high intensities which are desirable for high-quality fNIRS signal generation. On the other hand, their disadvantages (high heating problems, higher safety demands, large packaging, high costs and limited wavelength availability) forbid the usage of LDs in this mobile context and prioritize LEDs. As LEDs are small, comparatively cheap, a greater variation of NIR wavelengths is available, and the heating problems are less critical in the case of direct application to the head, they were judged more fitting for the design of this instrument.
Another very important advantage of LEDs for direct application on the head is the availability of multi-wavelength packages. Using the modified Beer-Lambert Law, it is

implicitly assumed that both interrogating wavelengths enter the tissue at the same spatial location to ensure the interrogation of the same partial tissue volume by both beams. So far, no multi-wavelength laser diodes with suitable NIR wavelengths were found. The use of multiple single-wavelength emitters makes optical fiber guides necessary to bring both signals together to a single output location. The use of optical fibers, however, does not fit the objective of this work.

For the multi-wavelength LED light sources, the two optimal NIR wavelengths had to be determined. As mentioned before, an optimal choice of the wavelength pair in the optical window is crucial for signal sensitivity and minimal crosstalk.
Generally, it is necessary to choose one wavelength above and one wavelength below the isobestric point of 805 nm in HbR and HbO absorption coefficients [20, 21] (see fig. 3.5).

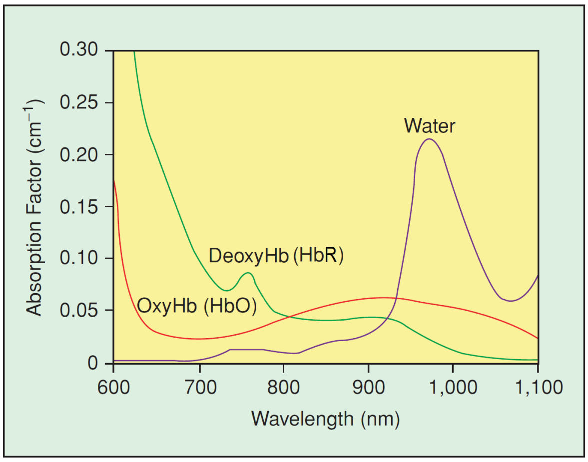

Figure 3.5: Absorption Coefficients of HbR, HbO and Water, taken from [14].

Left and right of the point at 805 nm, near isobestric wavelengths are commonly used to minimize absorption artifacts due to the presence of compounds other than hemoglobin [21]. To further narrow down the optimal wavelength pair, published investigations on the wavelength selection optimization problem, as well as the wavelength selections in NIRS instruments from both research and commercial developments were evaluated and summarized (see Appendix tab. A.3).
A commonly used wavelength is 830 nm, as the hemoglobin absorption spectra change little in the range of $830 - 900\,nm$ and the sensitivity of photo multiplier tubes (which were, as noted before, used for many of the first NIRS instruments) decreases rapidly above 840 nm [67]. Based on this early determination, many of the later investigations used 830 nm as a constant:

- Using an error propagation approach, Yamashita et al. [68] concluded that 830 nm together with $< 780\,nm$ is optimal.
- Using the Monte Carlo Method (Strangman), and empiric SNR tests (Sato), Yamashita, Sato and Strangman et al. [66, 68, 69] concluded that 830 nm with 690 nm or 760 nm minimize random and systematic errors.
- Using the Monte Carlo Method for minimizing crosstalk, Okui et al. [70] came to the conclusion that 830 nm with $690 - 750\,nm$ are optimal.

Uludag et al. [71], however, stated that $830\,nm$ is not the optimal wavelength and that > 730 and $< 720\,nm$ with both not $> 780\,nm$ should be used.
Finally, based on a three-layer model analysis, Correia et al. [72] concluded that $887 \pm 12\,nm$ and $704 \pm 7\,nm$ are optimal.

Table A.3 (see appendix) shows an overview of the wavelength pairs chosen in research and commercial NIRS instruments as well as the above-outlined results from theoretical investigations.

Based on this work, the wavelength pair $760 + 850\,nm$ was selected. Because of temporal non-availability in low amounts of LEDs with this wavelength configuration, alternatives had to be found and were compared (see A.10, appendix). As the best alternative, a $750 + 850\,nm$ LED from Epitex (L750-850-04A) in a $5\,mm$ molded package was selected and supplied by Meuvo-Technik Austria. The distance between both emitters in the LED is $< 1, mm$ and therefore negligible in this application context. Tab. 3.1 depicts the most important technical characteristics.

L750-850-04A	**750 nm**	**850 nm**
Maximum Power Dissipation	$200\,mW$	$160\,mW$
Typical Total Radiated Power ($I_F = 50\,mA$)	$15\,mW$	$18\,mW$
Max. Forward Current	$100\,mA$	$100\,mA$
Half Width $\Delta\lambda$ ($I_F = 50\,mA$)	$30\,nm$	$35\,nm$
Viewing Half Angle $\Theta_{1/2}$	$\pm 20\,deg.$	$\pm 20\,deg.$

Table 3.1: Epitex L750-850-04A characteristics.

3.4.2 NIR Light Sensor

Based on the comparison of photomultiplier tubes (PMTs), silicon photo diodes (SPDs) and avalanche photo diodes (APDs) (table 2.3, section 2.5), silicon photo diodes were selected for light detection in the fNIRS system. Because of their size and cost, PMTs are not a possibility for mobile devices. Although APDs can be used in principle, the necessity of high-voltage supply and cooling makes them less suitable for this application with regard to safety aspects and direct head attachment.
The very small packaging, high dynamic range and speed, together with low-voltage operation makes SPDs the best choice for mobile and adaptive lock-in amplification purposes. Another advantage is that they can be applied directly to the skin surface, which is the most efficient method of collecting the light [21]. The main disadvantage of SPDs is their low sensitivity due to a lack of internal gain. To minimize this drawback, only SPDs with integrated trans-impedance amplifiers (TIA) were taken into account during the investigation of available components. Using integrated and fitted TIAs should minimize noise pickup during the highly sensitive pre-amplification of the signal and compensate for the missing internal gain as much as possible.

Tab. 3.2 shows the most important characteristics of SPDs with integrated TIA that were available.
Due to the lock-in modulation of the optical signal, a bandwidth of several kHz is necessary. Therefore, some of the available SPDs are not suitable for lock-in purposes. From the remaining detectors, two were selected with respect to maximal sensitivity and minimal noise: ODA-5W-100K and OPT101. While the OPT101 has a ten times higher sensitivity, the ODA-5W-100K has a very high bandwidth. With OPT101 as favorite, both SPDs were tested in the further development process.

Model	Min. Supply Voltage $[V]$	TIA Gain $[\Omega]$	Typ. Sensitivity @ 850 nm $[V/\mu W]$	Max. Dark Offset $[mV]$	Typ. Dark Offs. Noise $[\mu Vrms]$	Cutoff Freq. $-3dB\ [kHz]$
ODC. ODA-5W-100K	± 5	$100\,k$	0.056	± 1	477	800
ODC. ODA-6W-100M	± 5	$100\,M$	56	± 2	198	1
ODC. ODA-5W-500M	± 5	$500\,M$	267	± 2	500	0.315
BB OPT101	$+2.7$	$1\,M$	0.6	$+10$	300	14
BB OPT301	± 2.25	$1\,M$	0.47	± 2	160	4
API SD112-42-11-221	± 5	$100\,k$	0.0558	± 1	60	750
API SD112-43-11-221	± 5	$75\,M$	45	± 3	20	1

Table 3.2: Silicon photo diodes with integrated TIA. ODC: Opto Diode Corp., BB: Burr Brown, API: Advanced Photonic Inc.

The OPT101 is a monolithic photodiode with single supply and integrated TIA operating in the photoconductive mode with an $1\,M\Omega$ feedback resistor and it has an effective sensing area of $2.29 \cdot 2.29\,mm^2$. Figure 3.6 shows the internal wiring and spectral responsitivity curve.

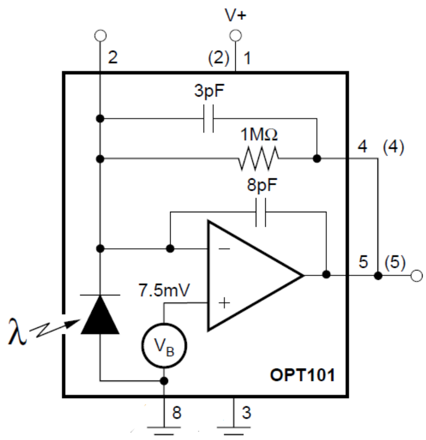

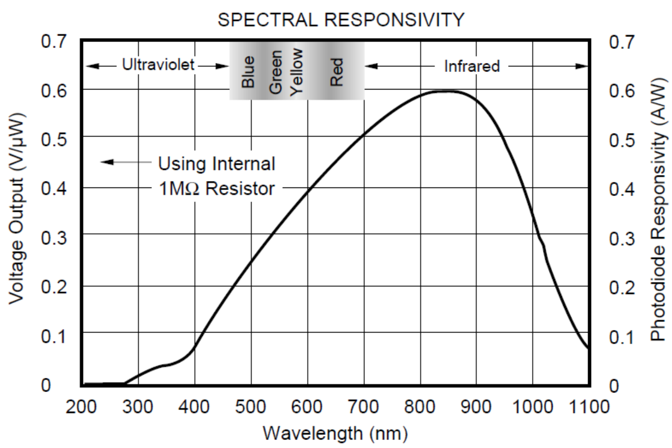

Figure 3.6: OPT101 interior circuit and spectral responsitivity curve, taken from OPT101 datasheet.

3.4.3 Amplification, Lock-In Modulation and Demodulation

As the NIRS signal is a very weak optical signal that can easily be drowned in noise during the extraction process, a lock-in approach was chosen for the system design. Lock-in amplification or phase-sensitive detection is a widely-used method for the recovery of weak signals masked by a strong noisy background, and can be found in many spectroscopic applications. In the following, the concepts of lock-in recovery will be briefly introduced to build a basis on which the system design can be further elaborated. For additional information on lock-in recovery, see for example the fundamental work of Meade [73, 74] which is also basis for the following explanations.

Lock-in amplifiers are based on the concept of phase-sensitive detection. Phase-sensitive detection is the demodulation of an ac signal with a common reference waveform. Demodulating the signal with the same reference waveform that was used for modulation, the phase-sensitive detector is only sensitive to signals coherent with the reference (same frequency and phase) and rejects others. Thus being an extremely narrow-band bandpass filter, it significantly enhances the signal-to-noise ratio (SNR):
Lock-in amplification results in large rejection of ambient room lighting sources, dark current of the photodetector, amplifier offsets and also of $\frac{1}{f}$ amplifier noise, implied that the signal is modulated at a fixed frequency in the kilohertz range, where the amplifier noise is significantly lower than at near zero frequency.

The mathematical description of this principle is quite straightforward:
Let $s(t)$ be the modulated signal carrying signal information in its amplitude $V_S(t)$ and $r(t)$ be the reference with constant amplitude V_R both with frequency ω and phase Φ

$$s(t) = V_S(t) \cdot \cos(\omega_S t + \Phi_S), \tag{3.10}$$

$$r(t) = V_R \cdot \cos(\omega_R t + \Phi_R). \tag{3.11}$$

Then demodulation (multiplication) of signal and reference yields

$$v(t) = \frac{V_S(t) V_R}{2} \cdot (\cos[(\omega_S + \omega_R)t + \Phi_S + \Phi_R] + \cos[(\omega_S - \omega_R)t + \Phi_S - \Phi_R]). \tag{3.12}$$

In case that signal and reference have the same frequency $\omega = \omega_S = \omega_R$ and a low-pass filter $A_L(\omega) = |H_L(j\omega)|$ is applied with cut-off frequency $f_c \ll \omega$, $A_L(0)$ being the magnitude of the filter response at zero frequency, the slow dc signal with frequency components $\ll f_c$ after filtering yields

$$v_{LP}(t) \approx \frac{V_R A_L(0)}{2} V_S(t) \cdot \cos(\Phi_S - \Phi_R). \tag{3.13}$$

$\cos(\Phi_S - \Phi_R)$ is the attenuation factor based on the phase between incident and detected optical signal and is mainly determined by the propagation delays of hardware components in the signal path.
In practice, the reference signal is often a square wave instead of a sine wave. In that case, the demodulation can be done simply by multiplication of the incoming signal with ± 1. Fig. 3.7 depicts this case.

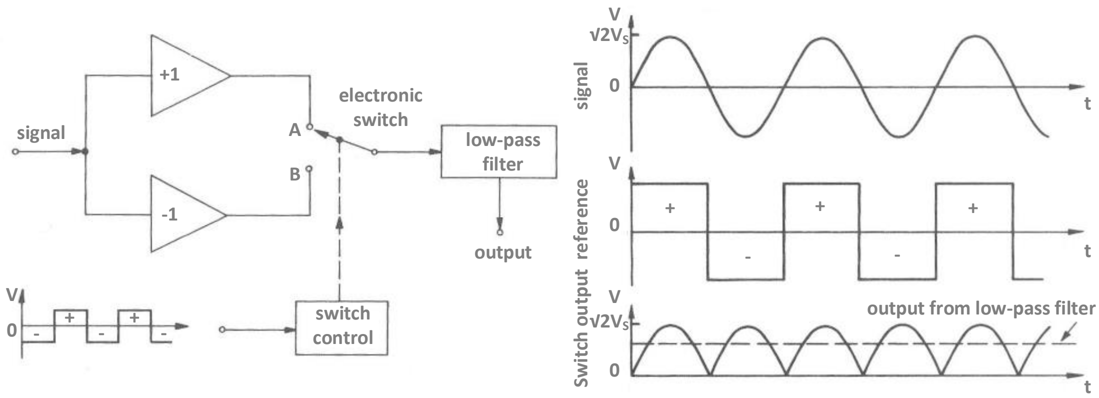

Figure 3.7: Principle of squarewave lock-in amplification, fig. taken from [73].

Using the same signal s(t) from eq. 3.10 now with a Fourier representation of the square wave reference r(t) for demodulation

$$r(t) = \frac{4}{\pi}[\cos(\omega_R t + \Phi_R) - \frac{1}{3}\cos(3(\omega_R t + \Phi_R)) + \frac{1}{5}\cos(5(\omega_R t + \Phi_R)) - ... \tag{3.14}$$

the resulting demodulated signal yields

$$\begin{aligned} v(t) = \frac{2V_S(t)}{\pi} \cdot [\cos(\omega_R t \pm \omega_S t + \Phi_R \pm \Phi_S) - \frac{1}{3}\cos(3\omega_R t \pm \omega_S t + 3\Phi_R \pm \Phi_S) \\ + \frac{1}{5}\cos(5\omega_R \pm \omega_S t + 5\Phi_R \pm \Phi_S) - ...]. \end{aligned} \tag{3.15}$$

Again, when the signal and reference have the same frequency $\omega = \omega_S = \omega_R$ and a low-pass filter $A_L(\omega) = |H_L(j\omega)|$ with cut-off frequency $f_c \ll \omega$, $A_L(0)$ being the magnitude of the filter response at zero frequency, is applied, the slow dc signal with frequency components $\ll f_c$ after filtering is

$$v_{LP}(t) \approx \frac{2V_R A_L(0)}{\pi} V_S(t) \cdot \cos(\Phi_S - \Phi_R). \tag{3.16}$$

As can easily be seen, the responses of the "ideal" sinusoidal synchronous detector (3.13) and the square wave reference detector (3.16) differ only in a constant scaling factor with the square wave excitation providing a 27% larger signal. "The essential difference in this case is that the phase-sensitive detector will also give a phase-sensitive dc output in response to signals at frequencies $3\omega_R$, $5\omega_R$, etc. A detection system with this property is said to be harmonically responding" (p. 35, [73]).
It has to be pointed out that this harmonic response is effective both on higher harmonics in the signal as well as on noise. The degradation by noise is, however, not as great as one could assume. As the noise in each additive term is random and not correlated with the signal, it "adds power only as the square root of its magnitude in each term, whereas the signal gained adds arithmetically" [75].
Again, the term $cos(\Phi_S - \Phi_R)$ is the attenuation resulting from a phase between the incident and the detected optical signal and is mainly determined by the propagation delays of hardware components in the signal path. A high delay results in a significant attenu-

ation of the signal during demodulation. Thus, all hardware elements in the signal path were chosen with respect to their speed/delay properties. A mathematical estimation and measurement of the real attenuation effects resulting from phase delay will be presented in subsection 4.1.4.

In the NIRS module, a 3.125 kHz square wave reference is produced by the PWM module of the microcontroller and is used for both modulation of the light sources and demodulation of the amplified detector signal. Fig. 3.8 depicts the application of lock-in amplification in the module.

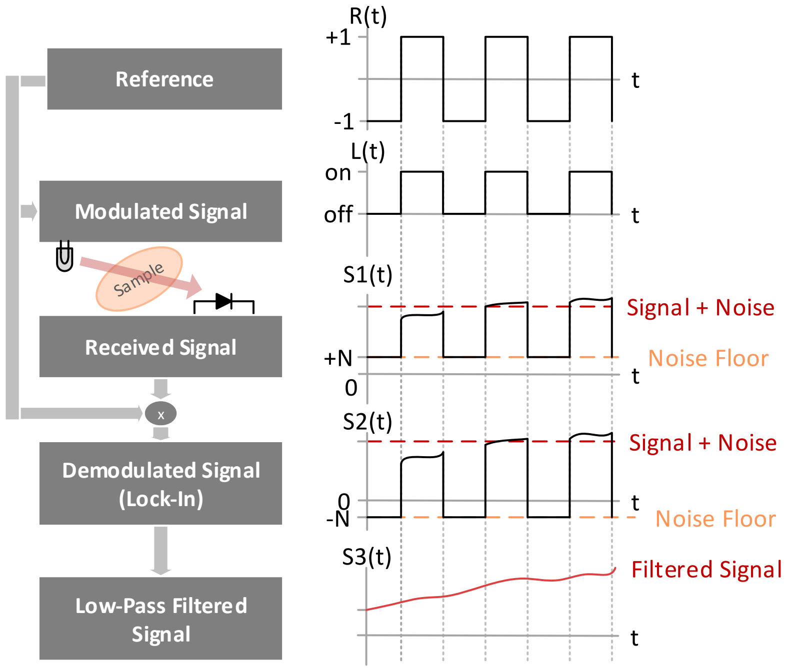

Figure 3.8: Principle of lock-in amplification in NIRS module.

The microcontroller PWM reference modulates the active channel's LED. The hardware details of this modulation are described in the next subsection on current regulators. The square wave optical signal is then sent into tissue for interrogation. On the detector side, the optical signal is received and amplified, now carrying both functional NIRS information and noise from stray light, dark current, amplifier noise and offset. This noise floor exists in both halves of the duty cycle: The active part carrying NIRS information (LED on), as well as the inactive part (LED off). Demodulating this signal with the PWM reference inverts the part of the signal only carrying the noise floor to a negative voltage level. Low-pass filtering the demodulated signal removes the high-frequency component, thereby integrating positive and negative voltage signals. Simplifying but vividly speaking, the low-pass filter subtracts the noise floor during LED-off times from the signal and noise during LED-on times. The lower the filter's cut-off frequency (respecting the physiol. signal's freq. spectrum), the narrower the lock-in bandwidth and thus the better the SNR.

For the actual lock-in demodulation, an integrated analog high-precision balanced modulator/demodulator circuit from Analog Devices was chosen.

The AD630 provides a $350\,kHz$ full-power bandwidth, $45\,V/\mu s$ slew rate, $-120\,dB$ crosstalk at $1\,kHz$ and a maximum channel offset voltage of $100\,\mu V$. It has been successfully used in low-cost laboratory lock-in applications [76] and in compact four-quadrant amplifier applications [77].

Figure 3.9 shows the hardware implementation of the complete detector amplification unit on the NIRS module.

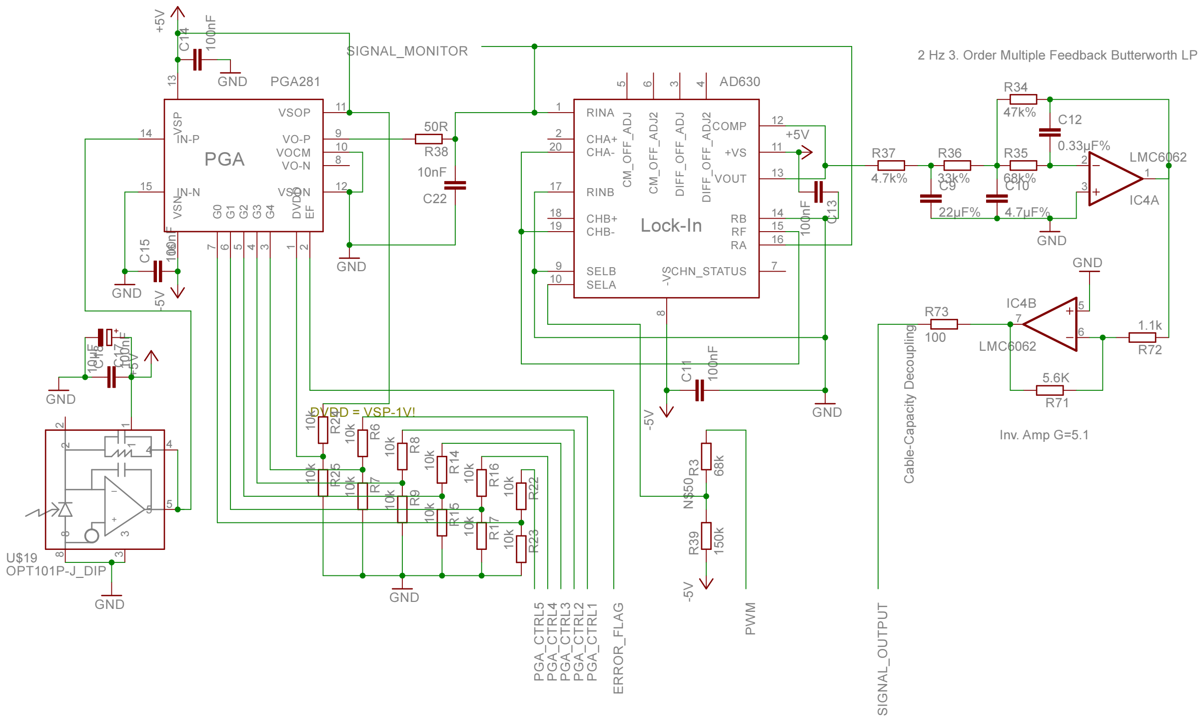

Figure 3.9: Hardware implementation of lock-in amplification.

On the bottom left, the OPT101 photodiode and integrated TIA detect and pre-amplify the optical signal. This signal is then fed into a programmable gain amplifier (PGA) for further amplification.
For this purpose, the high-precision instrumentation PGA281 from Texas Instruments was chosen. It provides near-zero long-term offset voltage and gain drift, very low $\frac{1}{f}$ noise of $420\,nV_{pp}$ at $f = 0.01 - 10\,Hz$, excellent linearity of $1.5\,ppm$ and binary gain steps from $\frac{1}{8}\,V/V$ to $176\,V/V$. As the digital supply voltage and gain control logic levels have to be lower than the input and output stage power supply levels due to internal design specifications of the PGA281, voltage dividers are applied to scale the digital logic levels from $+5\,V$ VDD down to $2.5\,V$ DVDD.
The amplified signal is then filtered with a passive RC output low-pass filter (R38 and C22) for removal of a minimal residual amount of high-frequency switching noise coming from the internal chopper stabilized architecture.
The filtered signal is monitored by the microcontroller (not in the picture) using a SIGNAL_MONITOR line and the PGA281 error flag line (EF) to enable gain adaption in case the signal reaches the dynamic range limit of the amplifier.

Now, the AD630 modulator/demodulator circuit demodulates the signal using the PWM reference from the microcontroller unit. In the internal design of the AD630, a voltage-sensitive comparator selects one of two input stages (inverting/non-inverting) based on the sign of the reference signal at the SELA pin. As the PWM signal is only positive or zero, a negative offset is applied by a voltage divider (R3, R39), shifting the 0 to +5V reference to a level 1.6V below zero, thus enabling the comparator to switch according to the PWM cycles.
The demodulator circuit is pin-configured with a gain of ± 2 to compensate for the factor $\frac{1}{2}$ resulting from the demodulation (see equations (3.13) and (3.16)).
The demodulated signal is then low-pass filtered by a 3rd-order multiple feedback Butterworth filter with cut-off frequency $f_c = 2\,Hz$ and finally inverted and amplified with a gain of $G = 5.1$. To this end, the LMC6062, a dual high-precision, low-offset voltage, micropower operational amplifier by Texas Instruments was selected. The LMC6062 provides a low-offset voltage of $100\mu V$, ultra-low input bias current of $10\,fA$ and operates single supply with ultra-low supply current of $16\,\mu A/Amplifier$. The filter design was simulated and optimized using LTSpice. Fig. 3.10 shows the simulated bode diagram of the filter and amplification unit.

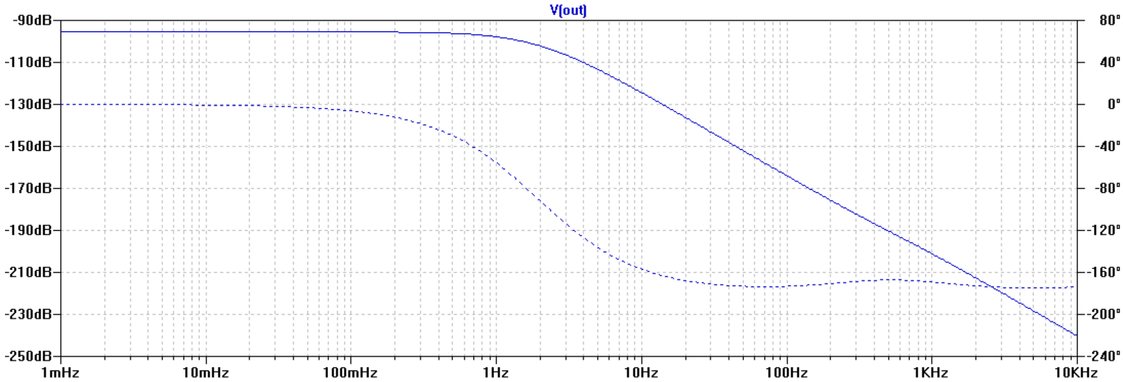

Figure 3.10: Low-pass and amplification bode diagram LTSpice.

The elements in this lock-in amplification unit were sequenced in a way that is thought to optimally utilize the advantages of the phase-sensitive detection technique. As the PGA amplifies the signal before demodulation, not only stray light, dark current and other noise effects during detection and pre-amplification but also offsets and amplifier noise from the process of post-amplification are reduced in the lock-in amplification process.
To keep the resulting signal as clean as possible, high-precision amplifiers are used for low-pass filtering and the final inversion and amplification.

3.4.4 Current Regulators

As mentioned in section 2.5, for high accuracy of the NIRS instrument the intensity of the emitted NIR LED light has to be kept as constant as possible, as emission variations can not be separated from absorbance variations in the signal after detection.
Even though a regulator using the measured emitted optical power as feedback variable would be optimal, the technical implementation of such a regulator increases system

complexity and is usually not necessary (see subsection 4.1.5 for drift evaluation). Thus, current regulators were designed to keep the current through the LED semiconductor junctions constant and independent from variations in supply voltage and temperature. At the same time, the design should be suitable for an adjustment of the current levels as well as square-wave modulation for lock-in purposes. For this, a basic approach proposed by Chenier 2007 [54] (see fig 3.11) was investigated:

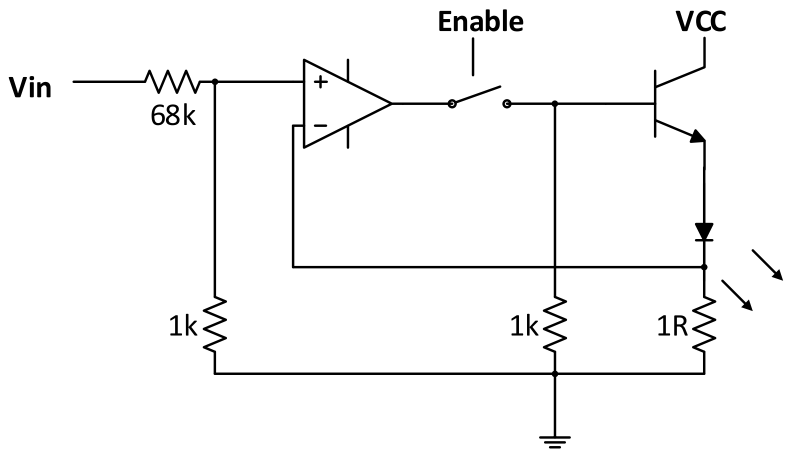

Figure 3.11: Current regulator by Chenier 2007 [54].

A reference input for the current regulation is produced by a voltage divider at the positive input of an operational amplifier (OpAmp). At the negative input of the OpAmp, the voltage drop across an $1\,\Omega$ resistor that is produced by the LED current is measured. Using the fundamental functionality of OpAmps, both potentials are subtracted, creating a difference voltage at the OpAmp output. This voltage controls the base/gate of a transistor, thus regulating the current flowing through it until the difference voltage is zero and the voltage at the positive OpAmp input and at the $1\,\Omega$ resistor are the same. For modulation, an analog switch is inserted between OpAmp output and the base of the transistor. When the switch is opened, the $1\,k\Omega$ pull-down resistor pulls the base to ground, thus closing the transistor.

When the proposed current regulator by Chenier was built and tested, however, it showed unstable and unreliable functionality. Therefore, a significantly changed and iteratively upgraded design is presented in this work (see fig. 3.12).

With the same regulation principle as described above, there are major differences in the design:

- The LED was placed directly at the power supply because of its three-pin multi-wavelength package. Having individual cathodes but a common anode, this was necessary to enable single-wavelength illumination.
- As the instability and unreliability of the design by Chenier was mainly based on the interruption of the closed loop control circuit, the analog switch for modulation was placed at the OpAmp input. With inverted logic (active low switch), the switch pulls the input to ground when the channel is inactive during short (modulation) or long (other channels active) LED-off times. This enables a continuous regulation, only changing the input reference variable.

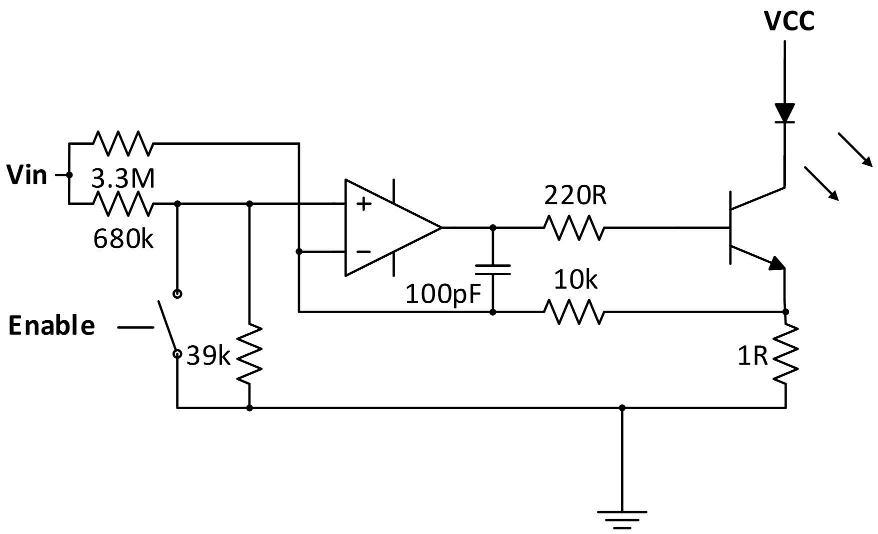

Figure 3.12: Developed and optimized current regulator for NIRS module.

- As the regulator is modulated in the kHz-range, over- and undershoots influence the ideally square-wave shape of the current. To enhance the switching performance, a passive RC negative feedback was added and evaluated (see section 4.1.3) and an output resistor was put between transistor base and OpAmp output to increase transistor gain and thus the effective slew rate.
- Despite the use of a high-precision OpAmp, evaluation of the regulator circuit revealed that during off-times (OpAmp inputs pulled to ground), some LED channels were still weakly illuminated. The small current flow leading to this illumination was found to be due to OpAmp offset voltage. This was corrected by impressing a low negative offset current to the negative OpAmp input with a $3.3\,M\Omega$ resistor that is connected with the reference input voltage V_{in}.

Figure 3.13 shows an excerpt of the hardware implementation on the NIRS module. For the sake of clarity, only two of eight NIRS channels (one multi-wavelength LED channel) are shown.
On the NIRS module, there are eight channels (4 dual wavelength LEDs) with corresponding current regulators. A 8:1 demultiplexer (MUX) is used to select the active channel and current regulator. By configuring the MUX for one channel, the PWM reference signal from the microcontroller is fed through to the corresponding analog switch of the current regulator that is to be activated. As the switches in this application use inverted logic (active low), the high-level part of the PWM duty cycle corresponds with an open switch and therefore an active current regulator/active current. The low part of the PWM cycle closes the switch which pulls the regulator input reference to ground, thereby closing the transistor and stopping the current flow.
For the MUX, the HEF4051B from NXP Semiconductors was chosen from several possibilities. The HEF4051B is an 8-channel analog multi-/demultiplexer with three address inputs, a common input, an active low enable input and eight independent ouptuts. Criteria for the selection of the analog MUX were mainly supply voltage and speed to keep the propagation delay in the signal path as low as possible and thereby minimize attenuation by the lock-in amplification process resulting from phase shifts. The

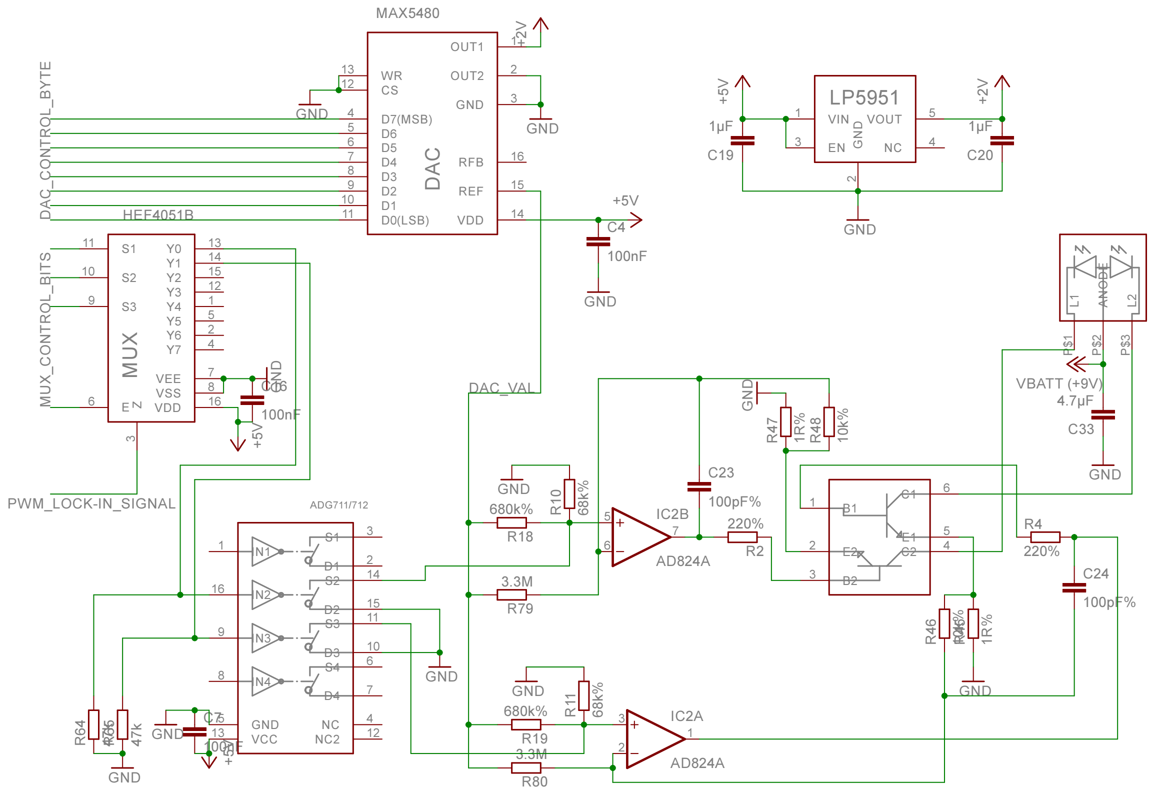

Figure 3.13: Excerpt of hardware current regulator implementation on the NIRS module.

HEF4051B's typical propagation delays for HIGH to LOW and LOW to HIGH propagation are $t_{PHL} = t_{PLH} = 15ns$.
For the analog switches, the low voltage quad CMOS switches ADG711 from Analog Devices were used. Providing four analog switches in one small TSSOP package, low on resistance of typ. 2.5Ω, low power consumption ($< 0.01\mu W$) and fast switching times ($t_{on} = 16ns$, $t_{off} = 10ns$), these switches fitted the requirements best. Again, criteria for the selection of the ADG711 were speed, supply voltage and power consumption. While in first design protoypes, based on the approach of Chenier 2007, the ADG712 with non-inverted logic was used, in the final NIRS instrument the ADG711 with inverted logic is used in the way described above. To keep the switch control inputs at defined logic levels during high-impedance output of the MUX (channel deactivated), pulldown resistors (R64, R65) are applied.

To adjust the NIR LED intensity, the current of the regulators is controlled by the reference voltage input that is produced by an $8\,Bit$ digital-to-analog converter (DAC). This DAC is configured by the microcontroller unit. At this time, four different LED power/current levels are implemented ($25\,mA$, $50\,mA$, $80\,mA$ and $100\,mA$). To this end, the MAX5480 $8\,Bit$ parallel DAC by Maxim Integrated Products was selected. It provides single supply operation, low power consumption of max. $100\,\mu A$ and a linearity of $\pm 1/2\,LSB$ over temperature in a small QSOP package. For use in voltage output mode, a reference input of $VDD - 3V, max$ has to be provided. This reference is generated by a micropower $2\,V$ buffered low-dropout CMOS voltage regulator (LDO) LP5951.

For the actual current regulators, two high-precision quad operation amplifiers, LMC6064 (Texas Instruments) and AD824A (Analog Devices), were used and evaluated (see section 4.1.3) with the AD824A showing the best characteristics due to a much higher slew rate and thus a higher edge steepness of the square-wave current signal. The AD824A is a quad, single supply, low power, rail-to-rail, FET Input OpAmp with very low input bias current of $2\,pA$, wide bandwidth of $2\,MHz$, a slew rate of $2\,V/\mu s$ and a low offset voltage of typ. $0.1\,mV$.
For the transistors in the current regulator design, general purpose FMB2222A npn arrays by Fairchild Semiconductor are used. In the FMB2222A, two transistors come in a tiny SuperSOT6 package, which allow a maximum continuous collector current of $500\,mA$ and a total power dissipation of $700\,mW$ with good switching characteristics (typ. delay time $t_d = 8\,ns$, rise time $t_r = 20\,ns$, fall time $t_f = 40\,ns$).

For the implementation of 8 NIRS wavelength channels on one module, one HEFB4051B MUX, two analog switch packages ADG711, one DAC MAX5480, two quad, high-precision amplifiers AD824A and four FMB2222A npn arrays are used.

3.4.5 Microcontroller Unit

An AtMega164A microcontroller from Atmel Corporation is used for PWM signal generation, control of MUX, DAC, PGA and for communication with the NIRS mainboard. The AtMega164 is a high-performance, multipurpose, low-power, $8\,Bit$ microcontroller with a $16\,kBytes$ in-system programmable flash memory, based on advanced RISC architecture. As the software design for the NIRS module microcontroller unit is described in subsection 3.7.1, only one important hardware design aspect will be further discussed at this point:
For the generation of the lock-in PWM square-wave reference, the built-in PWM channel is used with a 50% duty cycle at $3.125\,kHz$. As the internal $8\,MHz$ RC oscillator of the microcontroller provides only low precision in oscillation stability, a significant jitter can be observed in the spectral analysis of any produced kHz oscillation. For higher precision and to reduce this jitter, an external $20\,MHz$ crystal (type NX5032) is used for clock cycle generation of the AtMega164A. Wiring the microcontroller with an external crystal, its load capacity and the capacities of the conductor paths (strip lines) have to be regarded and additional capacities (C1, C2) have to be added for compensation (see fig. 3.14).

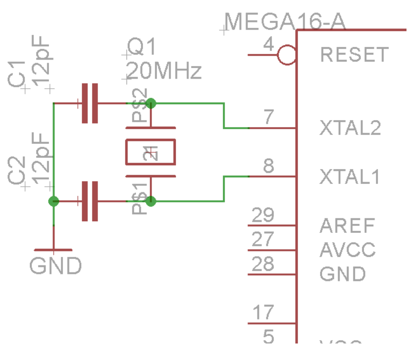

Figure 3.14: External clock source: crystal and capacities.

Using the expertise of a big online microcontroller community [78], the capacities were designed to be $12\,pF$ each with

$$C_1 = C_2 = 2 \cdot C_L - (C_P + C_I) \tag{3.17}$$

C_L being the load capacitance of the crystal, C_P the capacity of conductor paths, C_I the capacity of the microcontroller ports and $C_P + C_L \approx 5\,pF$.

3.4.6 General Remarks on Layout and Design

Generally, during the layout of the prototype and final PCB versions, much attention was paid to follow good design practice for measurement instrumentation design. Every supply pin of integrated components such as the microcontroller, photodetector, etc. is buffered with a $100\,nF$ capacity placed as closely as possible to minimize effects of power supply noise and fluctuations.
At the common anode of the NIR LEDs, $4.7\,\mu F$ capacitors are placed to buffer current peaks for the rising and falling edges during PWM current modulation.
To provide a stable ground (GND) potential without ground loops, shield top from bottom layer influences and vice versa, and to minimize effects on the supply voltage (VCC) during changes of load, a complete GND and VCC plane each are provided in a 4-layer PCB layout (see fig. 3.15).

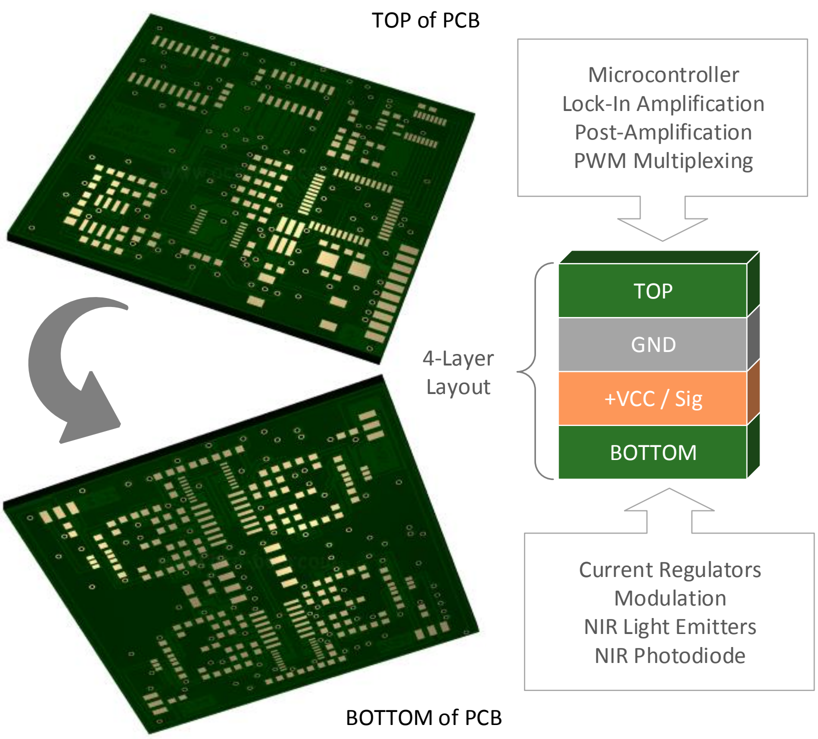

Figure 3.15: Layout of the NIRS module (using a PCB preview from www.pcb-pool.com).

Furthermore, functional units were separated to minimize electrical crosstalk:
With one exception, only the 8 current regulator circuits are placed on the bottom layer of the PCB. For detection of the optical signal, the OPT101 photodiode is also placed on the bottom layer and surrounded by regions on GND potential to shield from current regulator influences.
Electromagnetically isolated by the mid GND and VCC planes, the rest of the components is placed on the top layer. Thus, especially post-amplification, lock-in demodulation and filtering processes are shielded against electrical noise from current modulation processes. Sensible signal lines on all layers were routed as far away from potential noise sources as possible.
The complete layout of the fNIRS module is depicted in figs. A.5 and A.6 in the appendix.

3.5 Hardware Design NIRS Mainboard

In this section, the detailed implementation of the system concept's NIRS mainboard elements will be described. To do so, the functional units are viewed individually and implemented under consideration of the findings in earlier sections and using the results of evaluation and testing of 3 prototype versions that were designed in the course of this work.
For the full schematics, please refer to figs. A.7 and A.8 in the appendix.

3.5.1 Power Supply

All elements and integrated circuits on the NIRS module and mainboard were selected for low-voltage symmetric operation. To supply the NIR light emitters, detector, amplifiers, conversion and communication units with power, a dual $\pm 5\,V$ power supply was designed for the mainboard.
For mobility and safety reasons, batteries are used as power source. This has another great advantage: Since no rectification and filtering is necessary to get a clean dc output, the overall complexity of the power supply design is reduced.

An estimation of the maximum peak currents resulted in a minimum current of $200\,mA$ (consisting mainly of $100\,mA$ for the LED emission unit and $60\,mA$ for the Bluetooth module), that needs to be supplied without significant drop of the supply voltage.
As the availability of negative voltage, low-dropout regulators ($-5\,V$ rail) in this power range is very limited, common fixed-voltage regulators are used. Regarding efficiency, these are in fact not the optimal choice for battery-powered applications but were the best compromise so far. Step-down regulators were not considered as an alternative to preclude possible noise/error influences resulting from the high-frequency chopping process.

The dual power supply design that was implemented for the NIRS instrument (see fig. 3.16) is based on MC7805 and MC7905 $1\,A$ positive and negative voltage regulators from ON Semiconductor and the design considerations in the MC7900 and MC7800 series datasheets.
To ensure good high-frequency characteristics ($3\,kHz$ LED modulation) and stable operation under all load conditions, $10\,\mu F$ bypass tantalum capacitors with low internal impedance at high frequencies are placed directly at the regulator inputs. Further $100\,nF$